Absorption and quasiguided mode analysis of organic solar cells with photonic crystal photoactive layers

John R. Tumbleston,[1] **Doo-Hyun Ko,**[2] **Edward T. Samulski,**[2] **and Rene Lopez**[1*]

1 Physics and Astronomy Department, University of North Carolina Chapel Hill Chapel Hill, NC 27599, USA

2 Chemistry Department, University of North Carolina Chapel Hill Chapel Hill, NC 27599, USA

rln@physics.unc.edu

Abstract: We analyze optical absorption enhancements and quasiguided mode properties of organic solar cells with highly ordered nanostructured photoactive layers comprised of the bulk heterojunction blend, poly-3-hexylthiophene/[6,6]-phenyl-C61-butyric acid methyl ester (P3HT:PCBM) and a low index of refraction conducting material (LICM). This photonic crystal geometry is capable of enhancing spectral absorption by ∼17% in part due to the excitation of quasiguided modes near the band edge of P3HT:PCBM. A nanostructure thickness between 200 nm and 300 nm is determined to be optimal, while the LICM must have an index of refraction ∼0.3 lower than P3HT:PCBM to produce absorption enhancements. Quasiguided modes that differ in lifetime by an order of magnitude are also identified and yield absorption that is concentrated in the P3HT:PCBM flash layer.

OCIS codes: (230.5298) Photonic crystals; (350.6050) Solar energy.

References and links

1. C. W. Tang, "Two-layer organic photovoltaic cell," Appl. Phys. Lett. **48,** 183–185 (1986).
2. G. Li, V. Shrotriya, J. Huang, Y. Yao, T. Moriarty, K. Emery, and Y. Yang, "High-efficiency solution processable polymer photovoltaic cells by self-organization of polymer blends," Nature Mater. **4,** 864–868 (2005).
3. J. Peet, J. Y. Kim, N. E. Coates, W. L. Ma, D. Moses, A. J. Heeger, and G. C. Bazan, "Efficiency enhancement in low-bandgap polymer solar cells by processing with alkane dithiols," Nature Mater. **6,** 497–500 (2007).
4. W. Ma, C. Yang, X. Gong, K. Lee, and A. J. Heeger, "Thermally stable, efficient polymer solar cells with nanoscale control of the interpenetrating network morphology," Adv. Funct. Mater. **15,** 1617–1622 (2005).
5. V. D. Mihailetchi, L. J. A. Koster, J. C. Hummelen, and P. W. M. Blom, "Photocurrent generation in polymer-fullerene bulk heterojunctions," Phys. Rev. Lett. **93,** 216601-1–4 (2004).
6. D.W. Sievers, V. Shrotriya, and Y. Yang, "Modeling optical effects and thickness dependent current in polymer bulk-heterojunction solar cells," J. Appl. Phys. **100,** 114509-1–7 (2006).
7. J. D. Kotlarski, P. W. M. Blom, L. A. J. Koster, M. Lenes, and L. H. Slooff, "Combined optical and electrical modeling of polymer:fullerene bulk heterojunction solar cells," J. Appl. Phys. **103,** 804502-1–5 (2008).
8. M. Niggemann, M. Glatthaar, P. Lewer, C. Muller, J. Wagner, and A. Gombert, "Functional microprism substrate for organic solar cells," Thin Solid Films **511-512,** 628–633 (2006).
9. S. Rim, S. Zhao, S. R. Scully, M. D. McGehee, and P. Peumans, "An effective light trapping configuration for thin-film solar cells," Appl. Phys. Lett. **91,** 243501-1–3 (2007).
10. Y. Zhou, F. Zhang, K. Tvingstedt, W. Tian, and O. Inganas, "Multifolded polymer solar cells on flexible substrates," Appl. Phys. Lett. **93,** 033302-1–3 (2007).

#107125 - $15.00 USD Received 3 Feb 2009; revised 17 Apr 2009; accepted 21 Apr 2009; published 24 Apr 2009

11. M. Niggemann, M. Glatthaar, A. Gombert, A. Hinsch, and V. Wittwer, "Diffraction gratings and buried nano-electrodes–architectures for organic solar cells," Thin Solid Films **451–452,** 619–623 (2004).
12. S.-I. Na, S.-S. Kim, J. Jo, S.-H. Oh, J. Kim, and D.-Y. Kim, "Efficient polymer solar cells with surface relief gratings fabricated by simple soft lithography," Adv. Funct. Mater. **18,** 3956–3963 (2008).
13. J. Y. Kim, S.H. Kim, H. Lee, K. Lee, W. Ma, X. Gong, and A. J. Heeger, "New architecture for high-efficiency polymer photovoltaic cells using solution-based titanium oxide as an optical spacer," Adv. Mater. **18,** 572–576 (2006).
14. J. Gilot, I. Barbu, M. M. Wienk, and R. A. J. Janssen, "The use of ZnO as optical spacer in polymer solar cells: Theoretical and experimental study," Appl. Phys. Lett. **91,** 113520-1–3 (2007).
15. P. Bermel, C. Luo, L. Zeng, L. C. Kimerling, and J. D. Joannopoulos, "Improving thin-film crystalline silicon solar cell efficiencies with photonic crystals," Opt. Express **15,** 16986–17000 (2007).
16. D. Zhou and R. Biswas, "Photonic crystal enhanced light-trapping in thin film solar cells," J. Appl. Phys. **103,** 093102-1–5 (2008).
17. L. Zeng, Y. Yi, C. Hong, J. Liu, N. Feng, X. Duan, L. C. Kimerling, and B. A. Alamariu, "Efficiency enhancement in Si solar cells by textured photonic crystal back reflector," Appl. Phys. Lett. **89,** 111111-1–3 (2006).
18. L. Zeng, P. Bermel, Y. Yi, B. A. Alamariu, K. A. Broderick, J. Liu, C. Hong, X. Duan, J. Joannopoulos, and L. C. Kimerling, "Demonstration of enhanced absorption in thin film Si solar cells with textured photonic crystal back reflector," Appl. Phys. Lett. **93,** 221105-1–3 (2008).
19. D. Duche, L. Escoubas, J.-J. Simon, P. Torchio, W. Vervisch, and F. Flory, "Slow Bloch modes for enhancing the absorption of light in thin films for photovoltaic cells," Appl. Phys. Lett. **92,** 193310-1–3 (2008).
20. J. R. Tumbleston, D.-H. Ko, E.T. Samulski, and R. Lopez, "Electrophotonic enhancement of bulk heterojunction organic solar cells through photonic crystal photoactive layer," Appl. Phys. Lett. **94,** 043305-1–3 (2009).
21. J. R. Tumbleston, D.-H. Ko, R. Lopez, and E. T. Samulski, "Characterizing enhanced performance of nanopatterned bulk heterojunction organic photovoltaics," Proc. SPIE **7047,** 70470S-1–9 (2008).
22. D.-H. Ko, Department of Chemistry, University of North Carolina at Chapel Hill, Kenan Laboratories CB 3290, Chapel Hill, N.C. 27599, and J.R. Tumbleston, L. Zhang, S. Williams, J. DeSimone, R. Lopez, and E.T. Samulski are preparing a manuscript to be called "Photonic crystal geometry for organic solar cells."
23. T. Fujita, Y. Sato, T. Kuitani, and T. Ishihara, "Tunable polariton absorption of distributed feedback microcavities at room temperature," Phys. Rev. B **57,** 12428–12434 (1998).
24. R. Shimada, A. L. Yablonskii, S. G. Tikhodeev, and T. Ishihara, "Transmission properties of a two-dimensional photonic crystal slab with an excitonic resonance," IEEE J. Quantum Electron. **38,** 872–879 (2002).
25. S. G. Tikhodeev, A. L. Yablonskii, E. A. Muljarov, N. A. Gippius, and T. Ishihara, "Quasiguided modes and optical properties of photonic crystal slabs," Phys. Rev. B **66,** 045102-1–17 (2002).
26. V. D. Mihailetchi, H. Xie, B. de Boer, L. J. A. Koster, and P. W. M. Blom, "Charge transport and photocurrent generation in poly(3-hexylthiophene):methanofullerene bulk-heterojunction solar cells," Adv. Funct. Mater. **16,** 699-708 (2006).
27. G. Yu and A. J. Heeger, "Charge separation and photovoltaic conversion in polymer composites with internal donor/acceptor heterojunctions," J. Appl. Phys. **78,** 4510-4515 (1995).
28. P. W. M. Blom, V. D. Mihailetchi, L. J. A. Koster, and D. E. Markov, "Device physics of polymer:fullerene bulk heterojunction solar cells," Adv. Mater. **19,** 1551–1566 (2007).
29. F. Monestier, J.-J. Simon, P. Torchio, L. Escoubas, F. Flory, S. Bailly, R. de Bettignies, S. Guillerez, and C. Defranoux, "Modeling the short-circuit current density of polymer solar cells based on P3HT:PCBM blend," Sol. Energy Mat. Sol. Cells **91** 405–410 (2007).
30. H. Hoppe, N. S. Sariciftci, and D. Meissner, "Optical constants of conjugated polymer/fullerene based bulk-heterojunction organic solar cells," Mol. Cryst. Liq. Cryst. **385,** 113-119 (2002).
31. E. D. Palik, *Handbook of Optical Constants of Solids*. (Academic, 1985), pp. 369.
32. W. J. E. Beek, M. M. Wienk, M. Kemerink, X. Yang, and R. A. J. Janssen, "Hybrid zinc oxide conjugated polymer bulk heterojunction solar cells," J. Phys. Chem. B **109,** 9505–9516 (2005).
33. D. M. Whittaker and I. S. Culshaw, "Scattering-matrix treatment of patterned multilayer photonic structures," Phys. Rev. B **60,** 2610–2618 (1999).
34. L. A. A. Pettersson, L. S. Roman, and O. Inganas, "Modeling photocurrent action spectra of photovoltaic devices based on organic thin films," J. Appl. Phys. **86,** 487–496 (1999).
35. N.-K. Persson, H. Arwin, and O. Inganas, "Optical optimization of polyfluorene-fullerene blend photodiodes," J. Appl. Phys. **97,** 034503-1–8 (2005).
36. L. J. A. Koster, E. C. P. Smits, V. D. Mihailetchi, and P. W. M. Blom, "Device model for the operation of polymer/fullerene bulk heterojunction solar cells," Phys. Rev. B **72,** 085205-1-9 (2005).
37. G. A. Buxton and N. Clarke, "Computer simulation of polymer solar cells," Modeling Simul. Mater. Sci. Eng. **15** 13-26 (2007).
38. G. Li, V. Shrotriya, Y. Yao, and Y. Yang, "Investigation of annealing effects and film thickness dependence of polymer solar cells based on poly(3-hexylthiophene)," J. Appl. Phys. **98,** 043704-1-5 (2005).
39. J. D. Joannopoulos, R. D. Meade, and J. N. Winn, *Photonic crystals: molding the flow of light*. Princeton University Press, 1995.

#107125 - $15.00 USD Received 3 Feb 2009; revised 17 Apr 2009; accepted 21 Apr 2009; published 24 Apr 2009

40. NREL, "Reference Solar Spectral Irradiance: Air Mass 1.5," http://rredc.nrel.gov/solar/spectra/am1.5/.

1. Introduction

The search for alternative energy sources in the 21st century is a growing academic and industrial pursuit. Rising costs of carbon-based fuels coupled with increased emissions has placed a greater demand on the clean energy sector. A promising energy source is photovoltaics (PV), which has traditionally been made from high purity, expensive crystalline silicon (c-Si). The high cost of c-Si has been a primary drawback in its large-scale application. The search for cheaper, high-performance materials first involved other thin film inorganic materials such as amorphous silicon. Organic semiconducting materials have also been explored since the progress of Tang who devised a 1% efficient organic solar cell [1]. The driving force behind organic thin film devices is the reduced cost that results from using cheaper materials that can be readily deposited on large areas. In particular, mono-junction devices with nanoscale bulk heterojunction (BHJ) organic blends have pushed device efficiency to around 5% [2, 3].

In general, the disordered nanoscale morphology of organic BHJ solar cells has presented challenges for these devices to reach their full potential. First, the BHJ blends have low electron and hole mobilities that can result in low fill factors [4]. Second, they suffer from a limited probability of exciton dissociation into free charge carriers at the BHJ donor/acceptor interface. For some blends, this is 60% at short-circuit [5]. Both the fill factor [6] and exciton dissociation probability [7] can be increased by reducing the thickness of the photoactive layer, which is beneficial to the electrical performance. However, thinner photoactive layers are antithetical to the absorption of photons, so the result is a fundamental trade-off in photovoltaic design.

In an attempt to circumvent this problem, light trapping has been explored in organic solar cells. Designs that rely on geometric optics enhance absorption by increasing the path length of light in the photoactive layer [8, 9, 10]. Others have incorporated diffraction gratings [11, 12] and optical spacers [13, 14]. These results have shown improvement, but greater light control has been shown theoretically [15, 16] and experimentally [17, 18] with photonic crystals in Si solar cells. Here, the physical parameters of the crystal can be adjusted to produce optical enhancements near the band edge of the photoactive material where absorption is weak. This has been shown theoretically for an ordered BHJ system with a low index of refraction contrast photonic crystal geometry [19].

Recently we have made theoretical [20] and experimental [21, 22] progress in realizing a photonic crystal photoactive layer with high index of refraction contrast that yields absorption enhancements of $\sim$17% over the full spectral range. Enhancements in electrical performance were also noted, so this geometry offers an alternative to the optical and electrical trade-off for planar devices that exists when choosing a photoactive layer thickness. The enhancements in the optical performance warrants detailed analysis of the absorption properties of photonic crystal nanostructured devices. In particular, quasiguided modes are excited due to the nanostructured photoactive layer, which is not possible for conventional planar cells. These modes have been observed experimentally [23, 24] and described theoretically [25] for simple optical systems, but have not been thoroughly described when excited in organic photovoltaics.

In this paper, we first investigate physical dimensions and optical properties for nanostructured devices with the BHJ blend, poly-3-hexylthiophene/[6,6]-phenyl-C61-butyric acid methyl ester (P3HT:PCBM), that lead to maximized absorption enhancements. Specifically, we vary both the nanostructure thickness and optical properties of the low index of refraction conducting material (LICM) that surrounds 1-D and 2-D nanostructured P3HT:PCBM. We determine an optimal nanostructure thickness between 200 nm and 300 nm, while the LICM must have an index of refraction $\sim$0.3 lower than the BHJ blend. Second, we study the optical properties

#107125 - $15.00 USD Received 3 Feb 2009; revised 17 Apr 2009; accepted 21 Apr 2009; published 24 Apr 2009

of quasiguided modes where it is observed that both broad (short lifetime) and sharp (long lifetime) modes exist in nanostructured devices by comparing spectral absorption to photonic band diagrams. Lastly, we present profiles of exciton creation for a nanostructured device, which indicate that exciton formation is concentrated in the P3HT:PCBM blend flash layer above the nanostructured layer for quasiguided modes.

2. Theoretical approach

2.1. Materials and structure

P3HT:PCBM has shown efficiencies approaching 4.5% [2] and is one of the highest performing materials to date in the BHJ class of organic PV. Even though this blend does not suffer as severely from some of the morphology-related electrical processes mentioned above [26], any further improvement could boost the efficiency beyond 5%. Furthermore, the optical properties of other BHJ blends are very similar to P3HT:PCBM, so many of the results presented here could be applied to these materials. To briefly summarize, BHJ devices [27] contain a phase-separated blend of an electron donor (P3HT) and electron acceptor (PCBM). Upon photon absorption, a bound electron-hole pair, or exciton, is created. The exciton must diffuse to an interface between the electron donor and electron acceptor where it has some probability to split into a free electron and hole. The phase separation must be close to the exciton diffusion length ($\sim$10 nm [28]) in order to generate high free carrier concentrations. Free carriers then drift and diffuse through percolation pathways to their respective electrodes for collection.

The complex dielectric function of P3HT:PCBM and all other device materials are required as input in the optical models we present. Optical properties were measured using variable angle spectroscopic ellipsometry and showed agreement with literature values (P3HT:PCBM [29, 20]; glass, indium tin oxide (ITO), poly(3,4-ethylenedioxythiophene):poly(styrenesulfonate) (PEDOT:PSS) [30]; aluminum (Al) [31]). Due to the small phase separation of P3HT and PCBM as a BHJ, it is measured as a homogeneous layer because the phase separation is near two orders of magnitude smaller than the incident light. Fig. 1 shows the device designs where P3HT:PCBM comprises one of the materials in the nanostructured layer for 1-dimensional (1-D) and 2-dimensional (2-D) periodic photonic crystal solar cells. The other nanostructured material is a LICM, which is a transparent electron transport layer with low refractive index compared to P3HT:PCBM ($n_{LICM} \approx 1.4$ for all studies unless otherwise stated). Titanium oxide (TiOx) [13] and nanocrystalline zinc oxide (nc-ZnO) [32] are candidates for this material where we have used nc-ZnO [20, 21, 22]. The glass substrate, ITO, PEDOT:PSS, and LICM have negligible absorption for the spectral range of interest ($400 \leq \lambda \leq 685$ nm) and are taken to be fully transparent. On the other hand, the Al cathode is modeled with its true complex dielectric function, so optical losses do occur in this material. All absorption plots presented describe the fraction of incident light that is absorbed in the P3HT:PCBM only, where an absorption value less than 1 signifies loss from absorption in the Al or reflection/scattering. All materials are also assumed to be isotropic. P- and s-polarized light are incident normal to the relatively thick (1 mm) glass substrate where reflection from the air-glass interface is disregarded. This loss is 4% and approximately constant for all wavelengths.

2.2. Calculation method

The photonic properties of the nanostructured PV devices discussed in this paper are studied using transfer and scattering matrix methods with plane wave expansions [25, 33]. These methods are fast algorithms that calculate the optical properties and quasiguided eigenmodes in periodic photonic crystal slabs of finite thickness. Maxwell's equations are solved as an eigenvalue problem via plane-wave decomposition in two-dimensional Cartesian coordinates, and the solution is propagated across the different layers by means of scattering matrices, which define

#107125 - $15.00 USD Received 3 Feb 2009; revised 17 Apr 2009; accepted 21 Apr 2009; published 24 Apr 2009

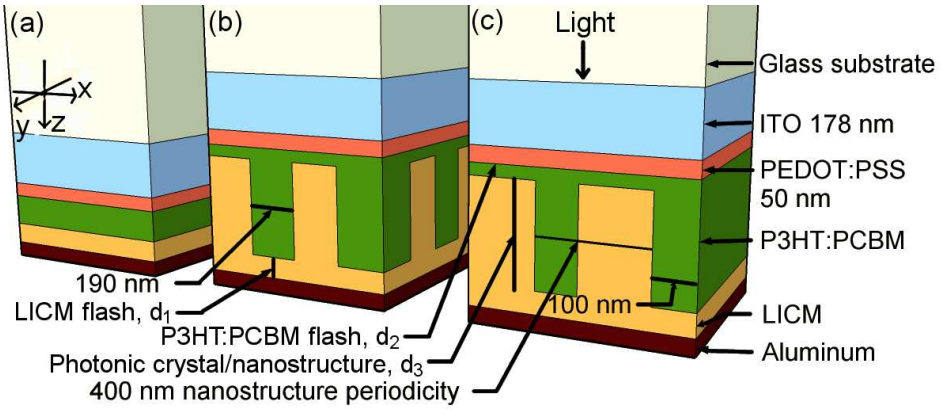

Fig. 1. Illustration of three photovoltaic devices studied: (a) Conventional planar control stack, (b) 2-D periodic posts with 395 nm square periodicity, and (c) 1-D periodic channels with 400 nm periodicity. S- and p-polarized light have electric fields oriented in y- and x-directions, respectively. The LICM flash thickness, d_1, P3HT:PCBM flash thickness, d_2, and nanostructure thickness, d_3, will be changed for optimization while all labeled values remain constant.

the continuity conditions for electromagnetic field components at each interface. The periodic symmetry of our proposed photonic structures makes them especially suitable for this approach. The in-plane periodicity of the structure is represented by the Fourier transform of the piece-wise dielectric permittivity. From this formulation, the reflection, transmission, absorption, and deflection coefficients are calculated for the entire stack for both s- and p-polarized light.

Along with these coefficients, the electromagnetic field profile inside the device is required to determine the location and density of exciton creation that follows the energy dissipation profile, $Q(x,y,z)$. In conventional planar devices, the field and energy dissipation profiles are only functions of depth in the device, z, and time [34, 35]. For our nanostructured designs, $\langle Q \rangle$ is a function of all spatial dimensions and is derived from Poynting's time-averaged continuity equation,

$$\langle Q \rangle + \nabla \cdot \left\langle \vec{S} \right\rangle = 0 \tag{1}$$

where $\left\langle \vec{S} \right\rangle$ denotes the time-averaged Poynting vector. This equation leads to the time-averaged monochromatic pointwise energy dissipation per unit time per unit area,

$$\langle Q \rangle = \frac{\pi c \varepsilon_0 \varepsilon_2 \left| \vec{E} \right|^2}{\lambda} \tag{2}$$

where ε_2 is the imaginary part of the dielectric function, ε_0 is the permittivity of vacuum, c is the speed of light in vacuum, λ is the free space wavelength, and $\left| \vec{E} \right|$ is the magnitude of the complex electric field. To calculate $\langle Q \rangle$, the fields are needed over a high resolution mesh in the unit cell. Using the transfer method [25], this can be done by first solving for the plane-wave amplitudes for the entire structure,

$$\begin{pmatrix} F_{sub}^{+} \\ F_{sub}^{-} \end{pmatrix} = T_{tot} \begin{pmatrix} F_{inc}^{+} \\ F_{inc}^{-} \end{pmatrix} \tag{3}$$

#107125 - $15.00 USD Received 3 Feb 2009; revised 17 Apr 2009; accepted 21 Apr 2009; published 24 Apr 2009

where the column vectors are the amplitudes in the substrate and incident semi-infinite spaces connected via the system transfer matrix, T_{tot}, and plus (minus) refers to propagation toward (away from) the stack. The amplitudes can be calculated to a given depth, z, in the structure, z_0, by using $F_{inc}^{\pm}$ from Eqn. 3 and the transfer matrix calculated to the point of interest, T_{z_0},

$$\begin{pmatrix} F_{z_0}^{+} \\ F_{z_0}^{-} \end{pmatrix} = T_{z_0} \begin{pmatrix} F_{inc}^{+} \\ F_{inc}^{-} \end{pmatrix} \tag{4}$$

Energy dissipation is proportional to exciton creation, so $\langle Q \rangle$ may be thought of as the exciton creation profile in the photoactive region. In the case of P3HT:PCBM, a large fraction of excitons will create free electrons and holes [26]. In this way, the exciton creation profile gives the proximity and density of exciton formation within P3HT:PCBM along with an approximate profile of free carrier generation. An exciton generation profile is generated at each depth, z, in the P3HT:PCBM flash layer and nanostructured layer, so this profile may be integrated to compare absorption at various depths for different wavelengths and polarizations.

It is beyond the scope of this paper, but the exciton creation profile also offers input to the electrical transport model of BHJ solar cells [36]. For planar devices, this model is one-dimensional, but it would need to be extended to higher dimensions [37] to appropriately describe the photonic crystal geometry. This would provide a means to simulate performance factors such as short-circuit current, fill factor, open circuit voltage, and efficiency with regard to an altered static internal electric field for the photonic crystal structure.

As a final note, numerical issues can arise for certain systems when using the transfer method. Mathematically, it can be shown that the transfer and scattering methods are equivalent [25], but exponentially growing transfer matrix entries can occur that lead to numerical instability. This must be checked for a given system before using the transfer method to determine the electromagnetic fields and thus exciton creation profiles in the nanostructured photoactive region.

3. Results and discussion

3.1. Absorption analysis

The physical dimensions and optical properties of the nanostructured layer for the devices in Fig. 1 greatly affect absorption in the BHJ blend. The parameters presented here will be directly applicable to nanostructured devices with P3HT:PCBM as the photoactive material even though some general trends can be applied to other photoactive materials. First, there are considerations regarding the volume of P3HT:PCBM in the nanostructured and planar control devices. In order to compare a nanostructured device to control cell, the volume of P3HT:PCBM available for the nanostructured cell must equal the planar control blend volume. This volume restricts the possible periodicities and thicknesses of the nanostructured region along with the thickness of the P3HT:PCBM flash layer. The optimal P3HT:PCBM thickness for a flat conventional device with an optical spacer layer is $\sim$100 nm [13, 14] due to balanced absorption and free carrier transport for this thickness. It is our goal to enhance the absorption of a planar device with this approximate thickness through a photonic crystal photoactive layer.

Interference also plays a major role in absorption for thin film stacks where the total stack thickness is comparable to the wavelength of light. Varying thicknesses of any non-absorbing layer (ITO, PEDOT:PSS, or LICM) will cause the P3HT:PCBM absorption to fluctuate, so it is necessary to vary one of these thicknesses to maximize integrated absorption for both the nanostructured and planar control devices. We keep ITO (178 nm) and PEDOT:PSS (50 nm) thicknesses constant for all studies in order to compare our devices more closely with literature. Instead, the LICM flash thickness, d_1, for the nanostructured device and the LICM film thickness for the control cell are varied from zero to 500 nm. For each thickness of LICM, the

#107125 - $15.00 USD Received 3 Feb 2009; revised 17 Apr 2009; accepted 21 Apr 2009; published 24 Apr 2009

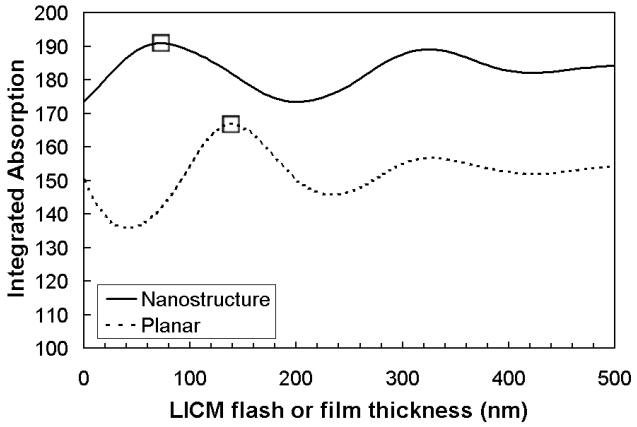

Fig. 2. Integrated absorption for varying thicknesses of LICM flash layer, d_1, for the 2-D periodic device and LICM optical spacer film for planar control. Comparisons between planar and control devices are made for LICM thicknesses that result in maximum integrated absorption (squares).

spectral absorption is integrated between $400 \leq \lambda \leq 685$ nm resulting in Fig. 2 for the 2-D periodic device with P3HT:PCBM flash thickness, $d_2 = 40$ nm, and nanostructured layer thickness, $d_3 = 300$ nm. The oscillation in integrated absorption occurs primarily due to interference where the electromagnetic field has varying strengths in the photoactive region. A correct optical comparison is made between nanostructured and planar control devices when both curves are maximized (as indicated by squares in Fig. 2). Integrated absorption is always greater for the nanostructured device, but using the lowest integrated absorption value for the planar device would result in incorrect and exaggerated absorption enhancements.

The first parameter to optimize is the ratio of P3HT:PCBM flash thickness, d_2, to nanostructure thickness, d_3. Keeping in mind that our goal is to enhance absorption for planar control devices with $\sim$100 nm thick P3HT:PCBM layers, both d_2 and d_3 are simultaneously varied for the 1-D periodic device while keeping all other parameters equal to those in Fig. 1(c). Here, the volume of P3HT:PCBM remains constant for each step in the optimization and equal to a control device with a P3HT:PCBM thickness of 115 nm. As previously discussed, the integrated absorption fluctuations due to interference are maximized for both nanostructured and planar control cells before calculating absorption enhancements. Fig. 3(a) shows absorption enhancements for s-, p-, and average polarization where the ratio between d_2 and d_3 is plotted as a function of d_2 and d_3. Due to the 1-D periodicity, s-polarization is more enhanced by the nanostructure than p-polarization. It can also be seen that a thin P3HT:PCBM flash layer with a thick nanostructure gives larger enhancements in absorption where the maximum for average polarization occurs for $d_2 = 15$ nm ($d_3 = 400$ nm). This would be the optimal value, but the fill factor has been shown to drop for very thin planar P3HT:PCBM cells with a photoactive thickness below $\sim$40 nm possibly due to decreased shunt resistance [38]. Even though the absorption enhancement drops around $d_2 = 60$ nm and increases to another maximum for $d_2 = 80$ nm, we take the flash layer value to be optimized for $d_2 = 40$ nm as it has the highest integrated absorption excluding the thin regime.

The thickness of the nanostructured region is another important parameter to optimize. Fig. 3(b) shows absorption enhancements for nanostructured thicknesses, d_3, from 100 to 500 nm for the 1-D periodic device with the optimized P3HT:PCBM flash thickness, $d_2 = 40$ nm. Varying the nanostructure thickness changes the volume of P3HT:PCBM, so each device is compared

#107125 - $15.00 USD Received 3 Feb 2009; revised 17 Apr 2009; accepted 21 Apr 2009; published 24 Apr 2009

to a planar control cell with equivalent volume. This shows that there exists a wide range of nanostructured layer thicknesses where absorption enhancements are observed. The p-polarized enhancement is maximized for $d_3 = 220$ nm while s-polarization is maximized for $d_3 = 290$ nm. Averaging the two polarizations produces an enhancement of 13% for $d_3 = 210$ nm. There is also reduced integrated absorption for thin ($d_3 < 130$ nm) and thick ($d_3 > 420$ nm) devices. Thicker nanostructures have reduced enhancement factors, because they are compared to planar control devices with thicker P3HT:PCBM film layers. For example, the nanostructured device with $d_3 = 500$ nm is compared to a planar control cell with 165 nm P3HT:PCBM film thickness, which is able to absorb almost all solar photons in the spectral range. In the case of thinner nanostructures, they do not produce the optical effects that lead to photonic enhancement. It is not shown here, but the 2-D periodic device is optimized for $d_3 = 300$ nm.

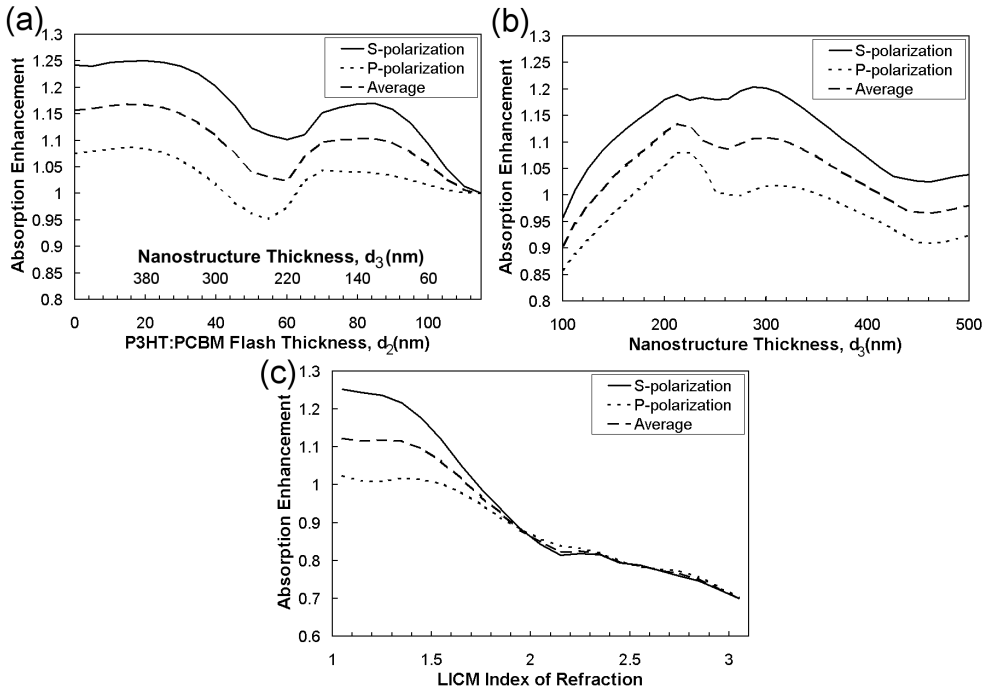

Fig. 3. Integrated absorption enhancements for variable (a) ratio of P3HT:PCBM flash thickness, d_2, to nanostructure thickness, d_3, (b) nanostructure thickness, d_3, and (c) LICM index of refraction of the nanostructured layer. The 1-D periodic device design is used in each optimization.

The final physical parameters to discuss are unit cell periodicity and P3HT:PCBM nanostructure width. Our choices are motivated by the desire to produce strong absorption enhancements near the band edge of P3HT:PCBM due to its weak extinction coefficient in this spectral range. A primary way to produce these enhancements is through quasiguided mode excitation [20]. These modes provide $\sim$20-fold enhancements for certain energy photons and will be discussed later in detail. Furthermore, as with nanostructure thickness, unit cell periodicity and nanostructure width also affect the thickness of P3HT:PCBM in the planar control cell. Values that give thick planar P3HT:PCBM layers are not desired, because these result in minimal absorption enhancements. The periodicity and index of refraction contrast (discussed below) provide the most control of the enhancement factors and spectral placement of quasiguided modes.

In terms of optical properties, the contrast in the dielectric functions of the two photonic

#107125 - $15.00 USD Received 3 Feb 2009; revised 17 Apr 2009; accepted 21 Apr 2009; published 24 Apr 2009

crystal materials in the nanostructured layer (P3HT:PCBM and LICM) has the greatest effect on overall absorption. A high contrast in the real part of the refractive index between these materials is desired to excite quasiguided modes. This is also a desirable trait for producing photonic band gaps in other systems [39]. To illustrate this concept, the LICM index is varied from $n = 1.05$ to 3.05 for the 1-D periodic device with $d_2 = 40$ nm and $d_3 = 300$ nm. Fig. 3(c) shows that the greatest enhancements occur when the LICM index of refraction is closest to unity and steadily decreases for increasing index. The average index of refraction of P3HT:PCBM for $400 \leq \lambda \leq 685$ nm is 1.94, so a minimum difference of $\sim$0.3 is needed between the two materials to produce enhanced integrated absorption. As with the above optimizations, there are larger absorption enhancements for s-polarization than for p-polarization. Furthermore, the LICM index must be lower than that of P3HT:PCBM. Even though the difference in index also exceeds 0.3 for LICM index values above 2.25, there is reduced absorption when compared to the planar control devices. Increasing the index to values greater than that of P3HT:PCBM causes greater reflection from the device due to sharper changes in the index from layer to layer. Quasiguided modes can still be coupled for large indices of refraction, but these enhancements are overshadowed by losses from greater reflection.

3.2. Quasiguided modes and band structure analysis

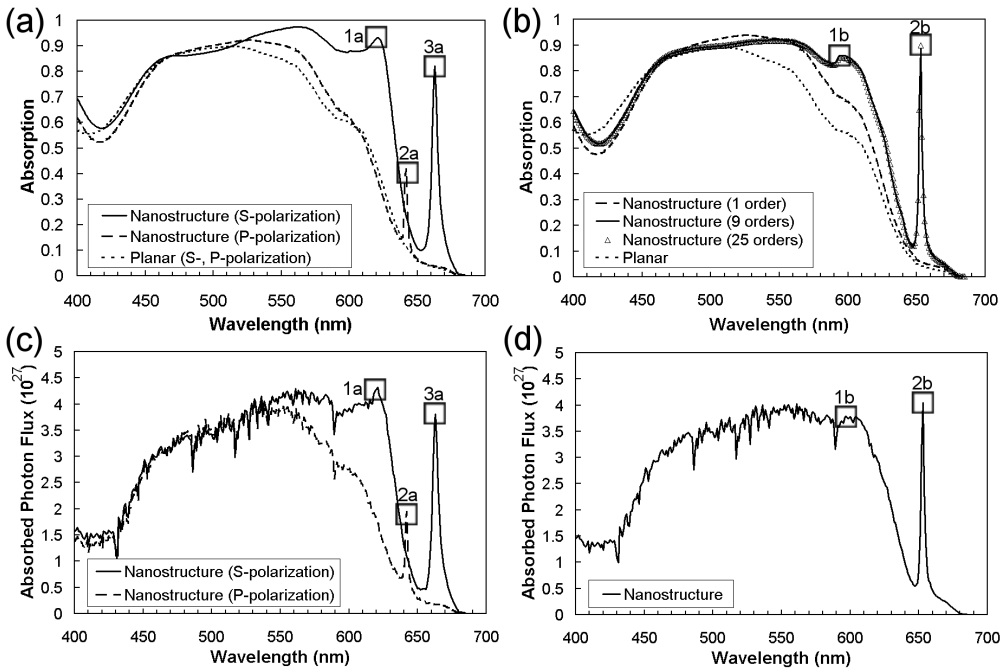

Fig. 4. Normal incidence absorption spectrum for (a) 1-D and (b) 2-D periodic nanostructured devices and comparable planar cells for both polarizations. P- and s-polarization for the 2-D periodic device are equivalent due to square symmetry. Quasiguided modes are labeled 1a, 2a, and 3a for the 1-D periodic cell, while modes for the 2-D periodic device are referenced 1b and 2b. Convergence of the solution method is also shown in (b) for one, nine, and twenty-five diffraction orders. The solution using one order corresponds to the main zeroth order. The AM 1.5 absorbed flux of solar photons ($\frac{1}{m^3 s}$) is presented for the (c) 1-D and (d) 2-D periodic cells to demonstrate the interplay between device absorption and the solar spectrum.

#107125 - $15.00 USD Received 3 Feb 2009; revised 17 Apr 2009; accepted 21 Apr 2009; published 24 Apr 2009

With the above noted set of physical parameters and optical constants, quasiguided modes are excited in the nanostructured solar cells. These modes are externally excited by incident light [25] and lead to sharp enhancements in absorption. Three quasiguided modes are shown in Fig. 4(a) in the normal incidence absorption spectrum for the 1-D periodic device that is near-optimal for s-polarized absorption ($d_1 = 70$ nm, $d_2 = 40$ nm, $d_3 = 300$ nm). The modes are labeled 1a, 2a, and 3a for reference. Furthermore, the optimal 2-D periodic device ($d_1 = 75$ nm, $d_2 = 40$ nm, $d_3 = 300$ nm) exhibits two modes at normal incidence as shown in Fig. 4(b). The quasiguided mode located at $\lambda = 652$ nm (mode 2b) is very sharp and offers an 18-fold absorption enhancement. Another mode exists further from the band edge at $\lambda = 595$ nm (mode 1b) that has a broader absorption spike. Mode excitation can also be observed when absorption is multiplied by the AM 1.5 solar photon flux [40] as shown for the (c) 1-D and (d) 2-D periodic devices. The solar photon flux reaches a maximum around $\lambda = 700$ nm, so the quasiguided mode excitations provide strong absorption near the highest flux region of the solar spectrum even though the extinction coefficient of P3HT:PCBM is small close to the band edge.

Fig. 5 shows the photonic band structure for the (a) 1-D and (b) 2-D periodic nanostructured devices. The observed modes in the absorption spectra of Fig. 4 for the Γ-point where $kx = ky = 0$ (normal incidence) are noted. The band diagrams are calculated by locating where the determinate of the scattering matrix for the system diverges [25]. This occurs for certain complex wavelengths. The imaginary part is related to the mode lifetime where modes with broader spectral width have shorter lifetimes. An absorption spike with no width would indicate an infinitely trapped waveguided mode. In the case of the 2-D periodic device, mode 1b is confirmed to have a larger imaginary part (shorter lifetime) than mode 2b by an order of magnitude, which is indicated by its broader spike in absorption.

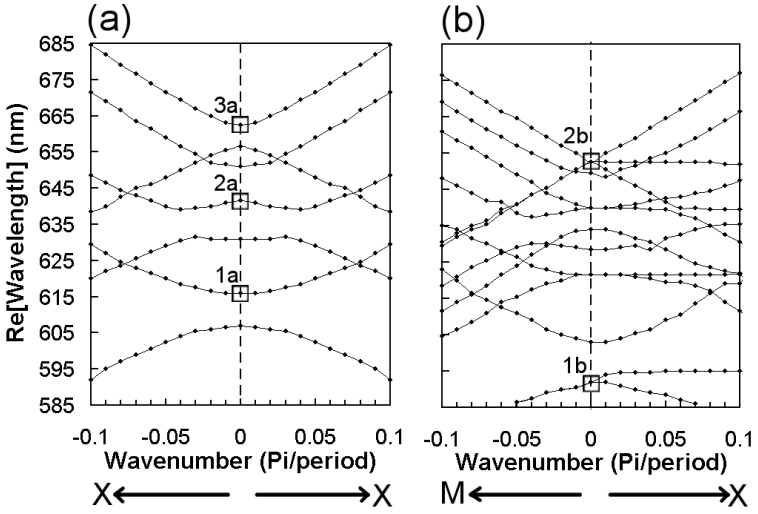

Fig. 5. Photonic band diagram for the (a) 1-D and (b) 2-D periodic nanostructured devices. Bands corresponding to optically active modes that result in quasiguided mode spectral absorption spikes for the Γ-point are referenced.

Figure 5(b) also indicates that there is two-fold and three-fold degeneracy at the Γ-point for the 2-D periodic device for the 1b and 2b modes, respectively. This degeneracy can be broken with non-normal incidence ($kx \neq 0$) giving rise to two s-polarized modes and one p-polarized mode for the case of mode 2b [20]. Further comparison of the spectral absorption (Fig. 4) with the band diagrams (Fig. 5) also reveals that there are more bands than quasiguided modes that

#107125 - $15.00 USD Received 3 Feb 2009; revised 17 Apr 2009; accepted 21 Apr 2009; published 24 Apr 2009

lead to absorption spikes. The bands resulting in absorption peaks are known as optically active modes, while those that do not are inactive [25].

Figure 4(b) also shows the convergence of the method, which helps characterize both quasiguided mode excitation and absorption enhancements. As previously mentioned, the simulation method used for solving Maxwell's equations is an approximation scheme that must be truncated after a certain number of terms in the Fourier series solution. These also correspond to a certain number of diffraction orders in Fourier space. After some number of orders, the solution converges. Taking only the zeroth order means that the nanostructured layer is treated as a homogeneous layer where the optical properties of the two materials (P3HT:PCBM and LICM in this case) are averaged by a weight proportional to their volume. It is clear that some of the overall absorption enhancement occurs for this order near the band edge. The physical process of scattering is not included for the zeroth order, so the enhancement only involves interference over a longer depth than for the planar case. It is also observed that the quasiguided modes are not excited, because they require the incident beam to exchange k-vectors with contributions in the lateral directions of the reciprocal lattice.

3.3. Exciton creation profiles

Along with studying the absorption and photonic band properties of these devices, the optical model can be further extended to determine the electromagnetic fields inside the photoactive region. This results in the profile of exciton creation, $\langle Q \rangle$, for the nanostructured and planar devices. The profiles are calculated at a given depth, z, where each slice varies over the two lateral dimensions, x and y. Figure 6(a) shows the profile for one unit cell of the 2-D periodic device ($d_1 = 75$ nm, $d_2 = 40$ nm, $d_3 = 300$ nm) at a depth of $z = 150$ nm into the nanostructured layer for $\lambda = 550$ nm. There is no energy dissipation around the post, because the LICM is transparent.

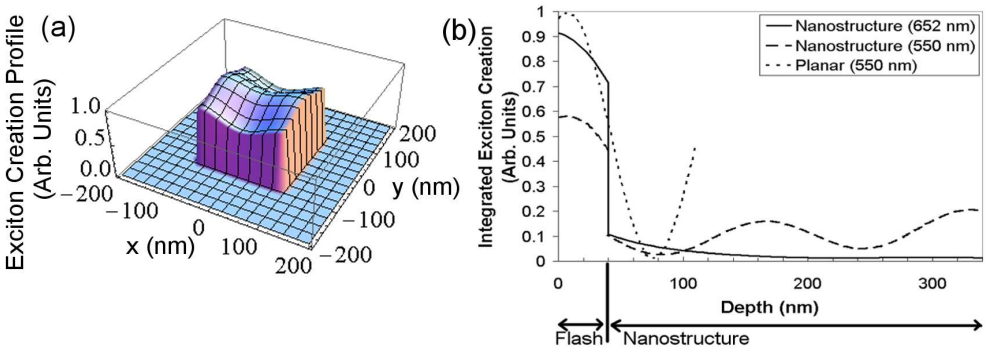

Fig. 6. (a) Exciton creation profile of one unit cell for the 2-D periodic device at a depth, z = 150 nm, into the nanostructured layer for $\lambda = 550$ nm. (b) Integrated exciton creation profile as a function of depth, z, for the 2-D periodic device for $\lambda = 550$ nm (general absorption) and $\lambda = 652$ nm (quasiguided mode 2b). The integrated exciton creation profile for the comparable planar device is also shown for $\lambda = 550$ nm.

Major differences in absorption profiles occur for wavelengths in and out of quasiguided mode resonances. Integrating the exciton creation profiles (Fig. 6(a)) over the lateral dimensions for each depth in the P3HT:PCBM flash and nanostructure layers yields Fig. 6(b) for both $\lambda = 652$ nm (quasiguided) and $\lambda = 550$ nm (non-quasiguided). Discontinuity occurs at the flash/nanostructure interface, because the complex dielectric function changes at the boundary due to the inclusion of both P3HT:PCBM and LICM in the nanostructure layer. From Fig.

#107125 - $15.00 USD Received 3 Feb 2009; revised 17 Apr 2009; accepted 21 Apr 2009; published 24 Apr 2009

4(b), both wavelengths yield comparable absorption ($\sim$90%) even though the former is due to quasiguided mode excitation and the latter results from the high extinction coefficient of P3HT:PCBM. Figure 6(b) shows that absorption as a function of depth is oscillatory in the nanostructured layer for $\lambda = 550$ nm, while it decays with depth for the quasiguided mode. The most striking feature is that greater absorption takes place for the quasiguided mode in the flash layer than for $\lambda = 550$ nm. Quantitatively, 79% of excitons are created in the P3HT:PCBM flash layer for $\lambda = 652$ nm, while only 39% are created there for $\lambda = 550$ nm. This may cause improved electrical performance for quasiguided modes due to high absorption in the thin $d_2 = 40$ nm flash layer where free carrier transport paths are relatively short [20].

Figure 6(b) also shows the integrated exciton creation profile for $\lambda = 550$ nm for the planar control device. For this wavelength, there is a greater concentration of excitons created toward the PEDOT:PSS side than the LICM layer. The depth where this concentration occurs will vary for different wavelengths, but the general shape of the curve is similar as has been shown in previous studies [14, 35].

4. Conclusion

We have presented the physical dimensions and optical properties that maximize integrated absorption for P3HT:PCBM bulk heterojunction organic solar cells with nanostructured photoactive layers. An optimal nanostructure thickness is determined to be 200-300 nm, while a minimal index of refraction contrast of $\sim$0.3 is required between the two nanostructured materials where the LICM index must be lower than that of P3HT:PCBM. Secondly, we have characterized the optical activity of excited quasiguided modes by identifying these modes in spectral absorption and photonic band diagrams. Both broad (short lifetime) and sharp (long lifetime) modes exist for the nanostructured devices. Exciton creation profiles for band edge quasiguided modes also indicate that these modes exhibit highly concentrated absorption in the P3HT:PCBM flash layer.

Acknowledgments

Two of the authors, Tumbleston and Lopez acknowledge support from the Army Research Office Grant No. W911NF-07-1-0539, while Ko and Samulski were supported by NSF (NIRT: Bio-Inspired Actuating Structures CMS-0507151) and NASA (URETI Biologically Inspired Materials Grant NAG-1-2301).

#107125 - $15.00 USD Received 3 Feb 2009; revised 17 Apr 2009; accepted 21 Apr 2009; published 24 Apr 2009